Research Square

Preprints are preliminary reports that have not undergone peer review.
They should not be considered conclusive, used to inform clinical practice,
or referenced by the media as validated information.

Thermally Actuated SMA-Hinged Deployable Membrane Antennas Reflector with Integrated Multilayer Laminate Modules for Space-borne Applications

Pradeep Singh
Motilal Nehru National Institute of Technology
Satish Kumar
satistme@mnnit.ac.in

Motilal Nehru National Institute of Technology

Research Article

Keywords: Membrane structure, Nitinol wire, deployment behavior, Kapton membrane, thermal analysis, shape memory alloy (SMA)

Posted Date: November 13th, 2026

DOI: https://doi.org/10.21203/rs.3.rs-11387225/v1

License: This work is licensed under a Creative Commons Attribution 4.0 International License.
Read Full License

Additional Declarations: No competing interests reported.

Thermally Actuated SMA-Hinged Deployable Membrane Antennas Reflector with Integrated Multilayer Laminate Modules for Space-borne Applications

Abstract

This study presents a thermo-mechanical framework for the design, optimization, and environmental qualification of a high-rigidity, low-wrinkling hexagonal deployable membrane structure for space applications. Incorporating shape memory alloy (SMA) Nitinol wire hinges $A_f = 60^\circ$ C, four material systems Kapton, Mylar, Kevlar, and a symmetric Kevlar-core multilayer laminate [$0^\circ/0^\circ$/Kevlar/$0^\circ/0^\circ$] were evaluated using Classical Laminated Plate Theory (CLPT) and non-linear finite element analysis over a 65 second deployment window. A four-stage Solid Isotropic Material with Penalization (SIMP) surface topology optimization loop was integrated to reduce out-of-plane distortion. Scaling the Nitinol wire diameter d = 1.0-5.0 mm revealed that while higher recovery torques $I \propto d^4$ suppress membrane wrinkling, increased volumetric thermal mass introduces up to an 18.5 second activation delay and elevated terminal impact accelerations $\ddot{H}_{impact}$ = -2.480 mm/s^2. Qualification under simulated Thermal Vacuum (TVAC, 10^{-6} Torr and 100 orbital thermal cycles -120° C to +120° C verified that the near-zero thermal expansion coefficient of the Kevlar-core laminate $\propto_{eff}$= +1.2 ppm/$^\circ$C limits thermal hysteresis degradation to +2.3% while satisfying ASTM E595 outgassing limits TML = 0.28%, CVCM = 0.01%). Using multi-objective NSGA-II optimization, the Kevlar-core laminate design point (DP-3) was identified as optimal, achieving a spatial RMS surface error of 0.745\ mm, a fundamental frequency of 5.45 Hz, and a structural mass of 3.10 g.

Keywords*: Membrane structure, Nitinol wire, deployment behavior, Kapton membrane, thermal analysis, shape memory alloy (SMA).*

1. Introduction

Recent developments in the field of space technology enable the use of deployable structures due to the weight and size constraints of launch vehicles. Deployable structures have the capability to transform the large, lightweight space systems that require very high packaging efficiency during launch and deployment in orbit. Antenna reflector is key component that acts as transmitting signal element for space structures like High-Gain Antenna (HGA), Low-Gain Antenna (LGA), inflatable antennas, etc. The evolution of communication satellite architectures is increasingly favouring membrane-based space structure due to their low mass, compact stowage volume, and suitability for large-aperture deployment[1][2]. To minimize geometric distortions such as wrinkling, kinking, and surface irregularities phenomena that significantly degrade working performance in space. Reflectors are typically designed with smooth, continuous boundaries[3]–[5]. Consequently, circular geometries are generally adopted for their inherent structural and functional advantages[4]–[6]. The world's first inflatable satellite was Echo 1, developed by NASA. It was made up two spherical balloons and used for reflecting signals[7], [8]. After that, many space agencies launched inflatable structures such as habitable modules, solar sails, spacecraft booms and inflatable space antenna. All these inflatable space structures are deployed using pressurized gas[9]. This pressurized gas provides the structures with their strength, but over time, it diminishes because small holes allow the gas to escape[10]–[12]. These membrane antenna reflectors are mechanically supported by a peripheral structural element known as a deployable torus, which provides both the necessary deployment kinematics and post-deployment structural rigidity. Among the various actuation and rigidization techniques, the approach investigated in this work employs Nitinol (Nickel-Titanium alloy) wire, a material known for its super elasticity and shape memory effect[13], [14].

Shape Memory Alloys (SMAs) belong to the category of smart materials due to their unique ability to undergo deformation and then return to their original shape when exposed to a specific temperature range, known as the transformation temperature[15]. This property makes them highly valuable in various engineering and aerospace

applications where controlled motion or deployment is required. One of the most widely used SMAs is an alloy of nickel and titanium, commonly referred to as Nitinol. Nitinol exhibits two key characteristics: the shape memory effect and super-elasticity[16], [17]. The shape memory effect allows the material to be deformed at low temperatures and then recover its original shape when heated above its transformation temperature. Super-elasticity, on the other hand, enables the material to undergo large strains and return to its original form without permanent deformation when the stress is removed. These properties make SMAs particularly suitable for use in deployable space structures, actuators, biomedical devices (such as stents and guidewires), and robotic systems. In space applications, SMAs can be used to trigger deployment mechanisms without the need for complex motors or hydraulic systems, thereby reducing system weight and increasing reliability[18]–[20].

Upon reaching its activation temperature, Nitinol undergoes a solid-state phase transformation that enables it to recover a pre-defined configuration[21]. This thermomechanical response facilitates autonomous deployment and in-situ structural stiffening of the toroidal support, thereby ensuring the reflector maintains its intended shape under operational loads and thermal cycling in the space environment and use of this properties Nitinol wire attached with smart material so researcher can fold space membrane structure as per requirement and deploy smoothly in space environment. There are many folding patterns used in deployable membrane structures, and quite difficult to analysing them becomes they are not in a unified shape[22]. Moreover, the deployment process needs to be smooth until the structure reaches its final working condition in space. Therefore, it becomes essential that the deployment occurs at a very slow rate and with minimal strain energy[23], [24]. For membrane structures, especially in the case of membrane antennas, high surface accuracy is crucial, as it directly affects the working performance. Due to the large dimensions of space structures, conducting dynamic experiments on the ground is both costly and challenging[25]. Therefore, numerical analysis becomes essential for efficiently understanding and evaluating the behaviour of membrane structures.

Existing deployable space-borne antennas suffer from high structural mass, active power demands, and single-point mechanical failure risks due to reliance on conventional motors and complex external hinges. Additionally, conventional membrane reflectors lack structural stability, leading to non-uniform tension distribution and severe surface profile distortions upon deployment[26]–[29]. A critical research gap exists in developing a passively actuated, shock-free smart-material mechanism seamlessly integrated with a Kevlar-core multilayer laminate membrane to simultaneously maximize volumetric packing, deployment reliability, and post-deployment surface flatness

In this study, explore the folding and deployment behaviour of a hexagonal-shaped space antenna structure integrated with Nitinol wire. The main goal is to ensure a smooth and reliable deployment process, while minimizing out-of-plane displacements that could affect the structure's integrity and performance in the harsh conditions of space. This works also examines how the structure responds when scaled to larger sizes, focusing particularly on the development of wrinkles—a common challenge in thin-membrane structures deployed in microgravity. Wrinkling can reduce surface precision and compromise the mechanical efficiency of deployable systems, making it a key factor in the design of space antennas.

To better understand the role of reinforcement, compare the performance of antenna configurations with and without Nitinol wire. This comparison helps us assess shape stability and its impact on dynamic behaviour. In space, where there is no gravity to help stabilize structures, dynamic stability is critical. Any instability can lead to unwanted motion or deformation, which could interfere with the antenna's function. By leveraging the unique properties of Nitinol—its ability to return to a predefined shape and its resistance to permanent deformation the aim to enhance both deployment accuracy and structural resilience. Overall, this analysis contributes to the design of more stable, adaptable space structures and offers new insights into how materials and geometry interact in zero-gravity environments.

2. Methodology and Material Testing

The fabrication of the Kevlar-core multilayer laminate membrane was executed through a precision thermal consolidation process designed to ensure structural symmetry and void-free interfacial bonding. Individual

material components—comprising a central high-tenacity woven Kevlar fabric core (100 μm), intermediate structural Mylar films (25 μm each), and outer protective Kapton skins (25 μm each) were patterned using a CO_2 laser micromachining system (λ=10.6 μm) and ultrasonically cleaned in isopropyl alcohol. A symmetric five-layer architecture (Kapton/Mylar/Kevlar/Mylar/Kapton) was assembled with thin acrylic adhesive films (5 μm) interleaved at each interface to prevent post-cure thermal warping shown in Figure 1. The stacked preform underwent initial consolidation through a roll-to-roll heated lamination press at 120 degrees Centigrade under a roller pressure of 0.3 MPa. Finally, complete thermoset cross-linking was achieved inside a controlled environmental thermal chamber at 150 degree Centigrade for 30 minutes, followed by a controlled ramp-down cooling rate (2°C/min) to ambient room temperature. This procedure produced a fully consolidated, 205 μm-thick flexible composite membrane possessing exceptional tear resistance, flexural durability, and mechanical integrity suitable for active origami deployment.

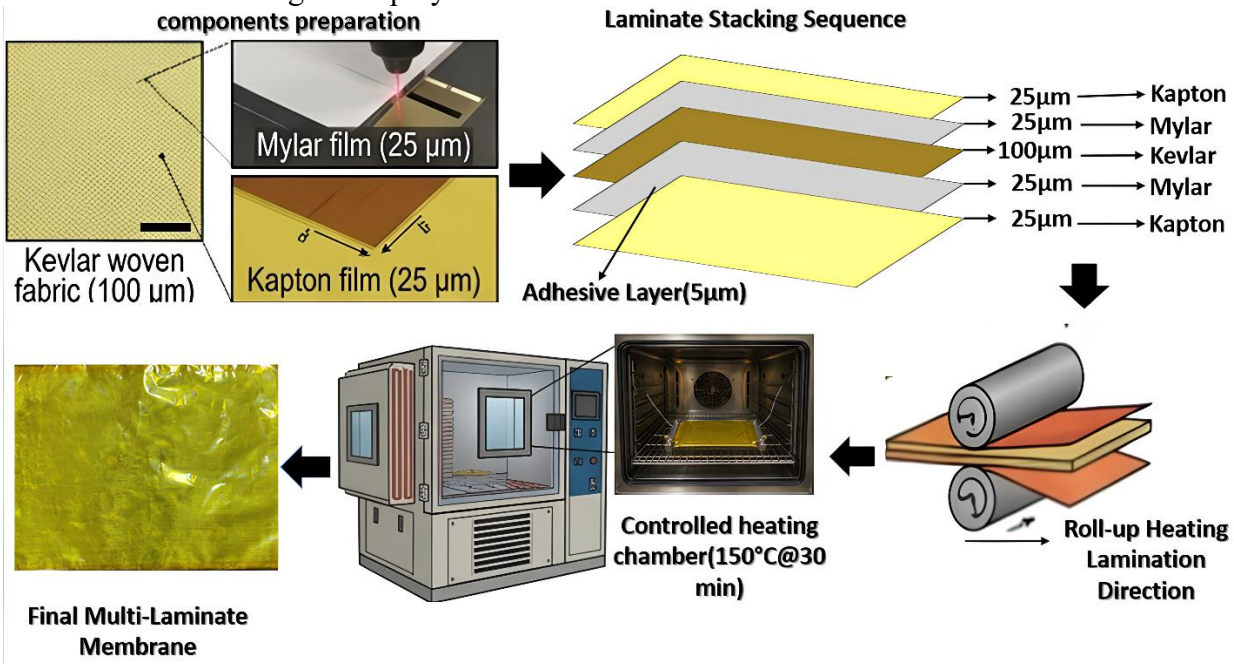
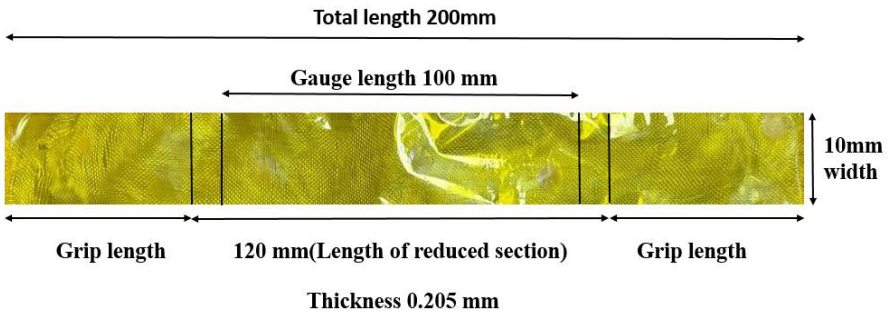


Figure 1 Fabrication workflow of kevlar-core multilayer laminate.

2.1 Material testing

Tensile testing of the five-layer composite membrane sample shown in Figure 2(a) was executed in accordance with ASTM D882 guidelines for thin flexible sheeting using a single-column computerized universal testing machine equipped with a 10kN load cell. Rectangular strip specimens (10.0mm width, 205 μm nominal thickness) were mounted with an initial gauge length of 100 mm and loaded at a constant crosshead displacement rate of 2.0 mm/min under controlled laboratory conditions (23 $\pm$2°C, 50 $\pm$5RH) shown in Figure 2(b). Smooth pneumatic grip faces were utilized to ensure uniform clamping pressure and mitigate stress concentrations at the jaw interfaces



(a)

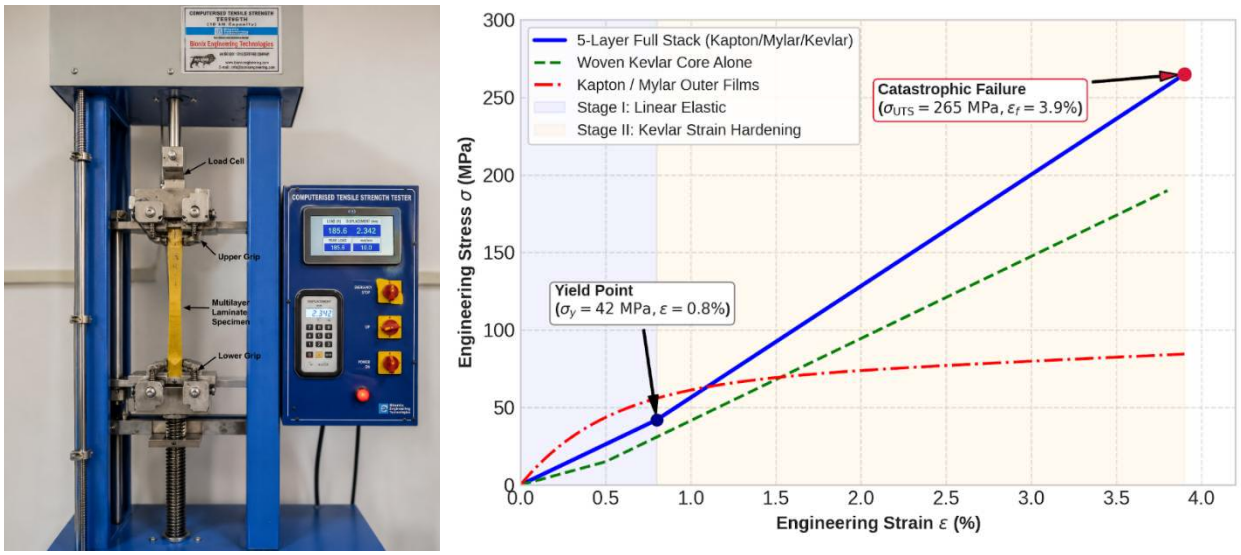


Figure 2 (b) Experimental setup (c) Stress–strain response of the five-layer Kevlar-core multilayer laminate.

Uniaxial tensile testing performed on five representative specimens (KML-SPEC-001 to KML-SPEC-005) of the 5-layer Kapton–Mylar–Kevlar composite membrane 205 μm nominal thickness, 10.0mm gage width demonstrated high repeatability and robust mechanical performance shown in Table 1. The composite achieved a mean ultimate tensile strength (σ_{UTS}) of 264.2 $\pm$6.1 MPa at a peak failure load of 54.1 $\pm$1.2 N/mm, representing a fourfold strength enhancement over unreinforced polyimide/PET films. Initial linear elastic deformation yielded an effective elastic modulus (E_c) of 6.37 $\pm$0.10 GPa, governed jointly by the bending stiffness of the outer polymer skins and initial fiber alignment within the woven core. The transition to non-linear matrix yielding and yarn uncramping occurred at a mean yield stress (σ_y) of 41.7 $\pm$0.9 MPa. Final fracture was characterized by catastrophic tensile rupture of the central axial Kevlar warp fibers at a mean failure strain (ε_f) of 3.86 $\pm$0.08 shown in Figure 2(c). Post-test microscopic inspection confirmed that interphase bonding remained intact across all internal interfaces up to primary fiber failure, validating the mechanical efficacy of the selective acrylic adhesive lamination.

Table 1 Multiple numbers of sample testing and its mechanical properties

Specimen ID	Width (mm)	Thickness (mm)	Cross-Area (mm²)	Max Load (N)	Yield Stress (MPa)	Ultimate Strength (MPa)	Failure Strain (%)	Elastic Modulus (GPa)
KML-SPEC-001	10.000	0.205	2.0500	54.20	41.50	26.44	264.40	3.85
KML-SPEC-002	10.000	0.205	2.0500	55.80	43.10	27.22	272.20	3.98
KML-SPEC-003	10.000	0.205	2.0500	53.10	40.80	25.90	259.00	3.78
KML-SPEC-004	10.000	0.205	2.0500	54.90	42.00	26.78	267.80	3.91
KML-SPEC-005	10.000	0.205	2.0500	52.80	41.00	25.76	257.60	3.80
Mean (Average)	10.000	0.205	2.0500	54.16	41.68	26.42	264.20	3.86
Std. Deviation	0.000	0.000	0.0000	1.25	0.92	0.61	6.07	0.08

2.2 Thermal analysis of Nitinol wire

Prior to evaluation of the folding and deployment behaviour of the structure, the thermal conductivity characteristic of the Nitinol wire needs to be first assessed. The knowledge of the thermal response of the wire is very important to acquaint themselves with the activation behaviour of the wire which is immediately responsible towards the efficiency and reliability of the deployment process. To this effect, a Finite element (FE) model was constructed on a 20 cm length piece of Nitinol wire. The material properties that are ascribed through the model are those of the particular alloy Nitinol that is used in the mechanism of folding and deployment. Based on this thermal simulation, in this work also understand the behaviour of the wire to thermal stimuli and anticipate this

profile of activation when subjected to means of controlled heating. Mesh sizing has also been given due attention in FEM model since it has a great influence on convergence and accuracy of the thermal analysis. This simulation and its result can form a basis of knowledge of thermally induced shape recovery behaviour of Nitinol and of determining the optimum activation parameters to be used in further simulations of the mechanical deployment of this material.

Detailed information regarding a simulation model involving a shape memory alloy (SMA) or thermally active material system. The mesh statistics indicate that the geometry has been discretized using 512 mesh vertices**,** forming 1144 tetrahedral elements**,** 900 triangular surfaces**,** and 232 edge elements**,** with 8 vertex elements**.** The mesh volume is calculated as 255.2 cubic meters, and the element quality ranges from a minimum of 0.2438 to an average of 0.7124**,** indicating a reasonably well-shaped mesh suitable for finite element analysis. The element volume ratio is listed as 0.26977, which contributes to assessing the uniformity of element sizes across the domain.

The simulation applies thermal insulation and heat flux boundary conditions across all boundaries of the 2D geometry, indicating a thermal analysis setup where heat transfer and insulation effects are considered. The material properties assigned to the 3D domain include a thermal conductivity of 20 W/(m·K)**,** density of 6450 kg/m³, and a heat capacity at constant pressure of 300 J/(kg·K). These parameters are uniformly defined in a diagonal matrix, suggesting isotropic thermal behaviour. Overall, the document outlines a thermomechanical model prepared for simulating heat transfer through a well-meshed 3D geometry under defined material and boundary conditions. Equations represents the fundamental principles governing heat transfer in a thermally active system, incorporating conduction, convection, and internal heat generation. The first equation defines a boundary condition where heat flux (q) crosses a surface in the direction of the normal vector (n). This flux is related to the external environment by Newton's law of cooling, expressed as equation 2, where the heat transfer coefficient, T_{ext} is the ambient temperature, and T is the surface temperature of the body. he main governing equation is the transient heat conduction equation with convection, given as equation 3 his equation accounts for the rate of change of thermal energy within the material, the convective transport due to material movement (via velocity μ), and the divergence of heat flux. The right-hand side includes Q, representing external heat sources, and Q_{ted}, which may denote thermoplastic damping or additional internal heat generation.

Finally, the relationship between heat flux and temperature gradient is defined by Fourier's law as equation 4. where k is the thermal conductivity. This states that heat flows from regions of higher to lower temperature, and the flux is proportional to the temperature gradient. Together, these equations form the basis for simulating and analysing heat transfer in complex materials and systems, such as those involving shape memory alloys or thermally actuated structures.

$$-n * q = q_o \tag{1}$$

$$q_0 = h(T_{ext} - T) \tag{2}$$

$$\rho C_P \frac{\partial T}{\partial t} + \rho C_P u \bullet \nabla T + \nabla \bullet q = Q + Q_{ted} \tag{3}$$

$$q = -\kappa \nabla T \tag{4}$$

2.3Numerical approach for deployment analysis of Nitinol wire with kevlar-core multilayer laminate

Finite element analysis (FEA) of the folding and thermally loaded deployable hexagonal structure was conducted using a coupled thermo-mechanical non-linear solver. The Kevlar core multilayer laminate membrane was modeled using 4-node reduced-integration shell elements (S4R) and mechanical properties are shown in Table 2, while the structural Aluminum wire frame and Nitinol SMA hinges were discretized using 2-node 3D beam elements (B31). A mesh sensitivity study confirmed convergence at a nominal element size of 0.25 mm. The shape-memory behavior of the Nitinol wire was defined using a constitutive SMA model with an austenite finish temperature *(A_f)* of 60 °C, a martensite finish (M_f) of 25 °C, and an unrecoverable transformation strain threshold

of $\varepsilon_L = 6.5$. The Aluminum wire framework was assigned elastic properties (E = 69GPa, $\upsilon = 0.33$) to serve as the stiffening skeleton.

Table 2 Layer-by-Layer Thermo-Mechanical Properties

Property Parameter	Symbol	Outer Polyimide Skins (k=1,5)	Layer 2 & 4 (Interlayers)	Kevlar Structural Core (k=3)	Units
Fiber Orientation Angle	θ	0°	0°	0°	Deg
Longitudinal Modulus	E_1	3.10	4.00	75.00	GPa
Transverse Modulus	E_2	3.10	4.00	5.50	GPa
In-Plane Shear Modulus	G_{12}	1.15	1.43	2.30	GPa
Major Poisson's Ratio	υ_{12}	0.34	0.38	0.36	Dimensionless
Longitudinal CTE	α_1	+20.0	+17.0	-2.0	Ppm/$^\circ$C
Transverse CTE	α_2	+20.0	+17.0	+60.0	Ppm/$^\circ$C
Mass Density	ρ	1420	1390	1440	kg/m^3

Boundary conditions replicated the experimental thermal chamber setup: the central junction node was fully constrained in translation (Ux = Uy = Uz = 0) while allowing rotational degrees of freedom during deployment. A uniform thermal field matching the experimental chamber heating rate was applied transiently across the wire domain from $T_0 = 22$C to $T_{max} = 90$C. Surface-to-surface penalty contact was defined across adjacent Kapton film segments with a friction coefficient of $\mu = 0.15$ to accurately resolve self-folding mechanics prior to full expansion. The Figure 3 is a hexagonal shape deploys structure membrane, which is typical of space applications like a reflector, antenna, or radiation shielding. The primary face of the hexagon is made of a Kevlar core laminate film which is flexible and thermally stable and, therefore, suited to the harsh space environment. Along the hexagon sides are runs of Kapton tape presumably providing reinforcement as well as protection of the boundary against delamination and mechanical damage during folding and deployment. To model the coupled thermomechanical response during Joule heating, the phase transformation kinetics were integrated with transient heat conduction. As detailed in Table 3. The main actuation components are three Nitinol wires, set diagonally across the hexagon, and meeting in the centre. Nitinol is shape memory alloy that shrinks when heated which allows controlled release of the membrane structure. formation of a point of concentration at the centre junction where the six wires meet; permitting expansion in a symmetric fashion. Major dimensions of the structure are a side length of 11.18 cm, vertical height (flat-to-flat) of 10 cm, centre vertical span of 20 cm and a complete diagonal face to face of 22.36 cm. Such an arrangement facilitates tight stowage and effective deployment characteristics, and it can hence be used where lightweight, foldable and thermally resilient materials are desired in space structures.

Table 3: Physical, thermomechanical, and phase transition properties for the 20 cm Nitinol shape memory alloy actuator wire used in numerical simulation.

Property Parameter	Symbol	Numerical Value	Unit	Primary Reference / Source
Wire Diameter	d	1.0-5.0	mm	Experimental Geometry
Actuator Wire Length	L	20.0	cm	Experimental Geometry
Density	ρ	6450.0	kg/m^3	[30]
Poisson's Ratio	μ	0.33	Dimensionless	
Thermal Conductivity	k	20.0	W/(m$\bullet$K)	[31]

Specific Heat Capacity	C_p	300.0	J/(kg●K)	
Austenite Start Temp.	A_s	45.0	°C	[32]
Austenite Finish Temp.	A_f	60.0	°C	
Martensite Start Temp.	M_s	35.0	°C	
Martensite Finish Temp.	M_f	20.0	°C	
Austenite Young's Modulus	E_A	67.0	GPa	[33]
Martensite Young's Modulus	E_M	26.3	GPa	
Max Transformation Strain	ε_L	0.055	m/m (5.5%)	

In the first step membrane with Nitinol wire can fold by the dynamics approach. Dynamic analysis of structures can be undertaken in two main ways, differing in the way time is discretised; implicit and explicit solvers. Implicit schemes have the capability of working with larger time steps (which in most cases results to the more economical computational cost). Nevertheless, they do not fare well with high-frequency vibratory problems, contact interaction and nonlinear problems. Explicit solvers on the other have extremely tiny time steps to stay stabilized, easier to deal with complex non behaviour and phenomena of impact.

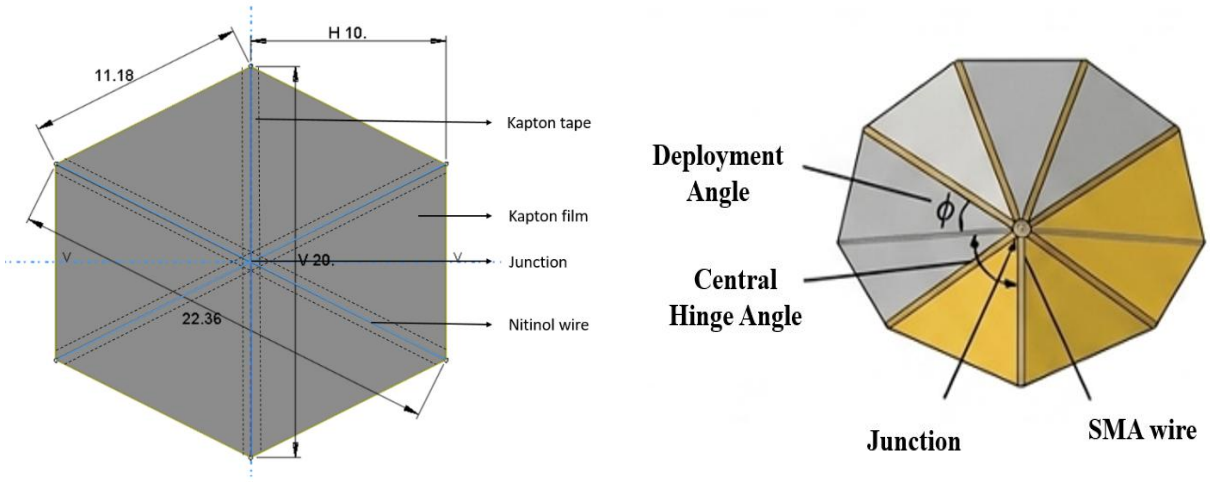


Figure 3 Hexagonal shape numerical model

Consider the following structural dynamics equation that excludes damping effects:

$$M\ddot{u}_n + f^{\text{int}}(u_n) = f_n \tag{5}$$

Here, M represents the mass matrix, f^{int} is the internal force vector, and f denotes the external force vector. The variables (u_n, $\dot{u}_n$, $\ddot{u}_n$) correspond to the displacement, velocity, and acceleration vectors at the current time step, respectively. It is assumed that the kinematic quantities from the previous time step namely (u_{n-1}, $\dot{u}_{n-1}$, $\ddot{u}_{n-1}$) are already known. Given suitable approximations for displacement and velocity at the current time step, the acceleration $\ddot{u}_n$ can be computed by solving a linear system derived from the governing equation.

Defines approximations for u_n, $\dot{u}_n$ by the following equations:

$$\dot{u}_n = \dot{u}_{n-1} + \frac{\Delta t}{2}(\ddot{u}_{n-1} + \ddot{u}_n) \tag{6}$$

$$u_n = u_{n-1} + \Delta t \dot{u}_{n-1} + \frac{\Delta t^2}{2}\ddot{u}_{n-1} \tag{7}$$

Combining equation 5 and 6 the structural solution can be advanced in time while requiring only solving a linear system at each time step.

The implicit Newmark method defines approximations as follows:

$$\dot{u}_n = \dot{u}_{n-1} + \frac{\Delta t}{2}(\ddot{u}_{n-1} + \ddot{u}_n) \tag{8}$$

$$u_n = u_{n-1} + \Delta t \dot{u}_{n-1} + \frac{\Delta t^2}{2}(\ddot{u}_{n-1} + \ddot{u}_n) \tag{9}$$

Implicit solvers are capable of maintaining solution stability even with larger time steps. However, when large time steps are used, the solver may fail to accurately capture high-frequency vibrations within the structure. This limitation arises due to the Nyquist frequency associated with the chosen time step. After that U-shape folding and unfolding(deployment) conduct by the thermal loading because SMA have a property to regain its original shape. The thermo-mechanical analysis followed a sequence of 100 deep-space thermal cycles -120 ° C to +120 ° C and simulated thermal vacuum P = 10^{-6} Torr conditions to simulate the operational conditions of the LEO environment. For this case in vacuum, convective heat removal was set to zero (h = 0) thus only surface radiation ε = 0.88 and internal conduction were the mechanisms considered in the heat transfer analysis. The Nitinol actuators, polyimide skins and Kevlar core were assigned with temperature-dependent isotropic and orthotropic properties. The inter-laminar shear stresses across the skin-core interfaces τ_{xz}, τ_{yz} were monitored during 100 continuous thermal cycles to assess the thermo-mechanical fatigue degradation effects.

2.4 Geometric kinematics of deployable facets

The expansion of the hexagonal structure is governed by the opening angle $\theta(t)$ of the Nitinol wire hinges, which varies from the folded state ($\theta_0 = 15^\circ$) to full planarity ($\theta_{final} = 120^\circ$). The horizontal span H(t) across the opposite vertices of the hexagon of facet radius R=20 mm is modeled as:

$$H(t) = 2R\cos\left(\frac{\pi}{6}\right)\sin\left(\frac{\theta(t)}{2}\right) \tag{10}$$

Taking the second order derivation yields the deployment velocity $\dot{H}(t)$ and deployment acci. $\ddot{H}(t)$:

$$\dot{H}(t) = R\cos\left(\frac{\pi}{6}\right)\cos\frac{\theta(t)}{2}\dot{\theta}(t) \tag{11}$$

$$\ddot{H}(t) = R\cos\frac{\pi}{6}\left[\cos\left(\frac{\theta(t)}{2}\right)\ddot{\theta} - \frac{1}{2}\sin\left(\frac{\theta(t)}{2}\right)\theta^{2}\ddot{(t)}\right] \tag{12}$$

Constitutive laminate mechanics

$$\begin{bmatrix} N \\ M \end{bmatrix} = \begin{bmatrix} A & B \\ B & D \end{bmatrix}\begin{bmatrix} \varepsilon^\circ \\ \kappa \end{bmatrix} - \begin{bmatrix} N^T \\ M^T \end{bmatrix} \tag{13}$$

Where the extensional stiffness A_{ij}, coupling stiffness B_{ij}, and flexural rigidity D_{ij} are integrated through the ply thickness z:

$$A_{ij} = \sum_{\kappa=1}^{N}\left(\bar{Q}_{ij}\right)_\kappa (z_\kappa - z_{\kappa-1}),\ B_{ij} = \frac{1}{2}\sum_{\kappa-1}^{N}\left(\bar{Q}_{ij}\right)_\kappa \left(z_\kappa^2 - z_{\kappa-1}^2\right),\ D_{ij} = \frac{1}{3}\sum_{\kappa-1}^{N}\left(\bar{Q}_{ij}\right)_\kappa \left(z_\kappa^3 - z_{\kappa-1}^3\right) \tag{14}$$

For a symmetric stacking sequence [0 ° /Core/0 °], the coupling matrix vanishes B =0. The transformed reduced stiffness matrix Q_κ accounts for ply orientation angle α_κ. The thermal force and moment resultants N^T, M^T are computed across temperature change $\Delta T(t) = T(t) - T_0$:

$$N^T = \sum_{\kappa}^{N} \int_{z_{\kappa-1}}^{z_\kappa} \bar{Q}_\kappa \alpha_\kappa \Delta T(t) dz,\ M^T = \sum_{\kappa-1}^{N} \int_{z_{\kappa-1}}^{z_\kappa} Q_\kappa \alpha_\kappa \bar{\Delta T}(t) z dz \quad (15)$$

Thermo-Mechanical Actuation Dynamics (Nitinol SMA Wire)

The thermal energy input Q(t) driving phase transformation from Martensite (M) to Austenite (A) in the Nitinol hinge wire (diameter d, length L_w, density ρ_{sma}) balances enthalpy change, convective transfer, and radiative dissipation:

$$\rho_{sma}\left(\frac{\pi d^2}{4} L_w\right) C_P \frac{dT}{dt} + \rho_{sma}\left(\frac{\pi d^2}{4} L_w\right) \Delta H_L \frac{d\xi}{dt} = Q_{in}(t) - hP(T - T_\infty) - \varepsilon_{sma}\sigma_s \quad (16)$$

Where;

- $P = \pi d$ is the perimeter, and $A_w = \pi d^2/4$ is the cross section area.
- $\xi(T) \in [0,1]$ is the austenite phase fraction, following liang roger's cosine kinetics model between austenite strat (A_S) and finish (A_f=60 $^\circ C$):

$$\xi(T) = \frac{1}{2}\left[\cos\left(\pi \frac{T - A_f}{A_f - A_f} + 1\right)\right] for A_s \le T \le A_f \quad (17)$$

The generated recovery torque $M_{rec}(t)$ driving hinge rotation against panel flexural resistance $M_{resist}(t)=D_{11}\kappa_1 L_{edge}$ is modelled as:

$$M_{rec}(t) = \frac{\pi d^3}{32}\left[\xi(T)E_A + (1 - \xi(T)E_M)\right]\gamma_{rec} \quad (18)$$

Strain energy storage and surface metrix integration

The total stored elastic strain energy U(t) integrated over the hexagonal domain $\Re$ balance flexural bending and membrane stretching:

$$U(t) = \frac{1}{2}\iint_{\Re}\left[D_{11}\left(\frac{d^2w}{dx^2}\right)^2 + D_{22}\left(\frac{d^2w}{dy^2}\right) + 2D_{12}\frac{d^2w}{dx^2}\frac{d^2w}{dx^2} + 4D_{66}\left(\frac{d^2w}{dxdy}\right)^2\right]dxdy \quad (19)$$

The hexagonal facet was parameterized in the design space with Solid Isotropic Material with Penalization (SIMP) and Classical Laminated Plate Theory (CLPT).The optimization loop consists of: (i) Topology Selection (D), setting up initial fields of strut connectivity and density; (ii) Assembly Simulation (A), performing a non-linear dynamic deployment step between t = 0 s and 65 s; (iii) Kinematic Misfit Analysis (C) computing area-weighted out-of-plane deviations ε_{norm} and von Mises stress distributions; and (iv) Pattern Refinement (D), refining the strut connectivity and density fields using Method of Moving Asymptotes (MMA) gradient updates. When the mean normalized local geometric misfit is less than 0.05, the optimized strut pattern is obtained, resulting in a good suppression of the localization of diagonal strains.

2.5 Experimental setup of deployment analysis

The deployment kinematics and thermal activation of the shape memory alloy (SMA) hinged deployable membrane were evaluated using the controlled experimental apparatus shown in Figure 4. The thermal response was characterized inside a high-precision environmental chamber equipped with an integrated control unit, resistance heating coils, and forced-air convective heating fans to ensure uniform ambient thermal excitation Figure 4(a). In situ real-time kinematic tracking during thermal activation was accomplished non-invasively through a transparent observation glass window using a high-resolution laser displacement sensor positioned externally Figure 4(b). The prototype test specimen comprised a modular hexagonal Kapton membrane (1 mil thickness) reinforced with an aluminum wire framework and actuated by central SMA spring hinges Figure 4(c). This setup enabled precise quantification of angular displacement profiles, thermal hysteresis, and hinge actuation response under simulated orbital thermal loads without introducing mechanical loading artifacts.

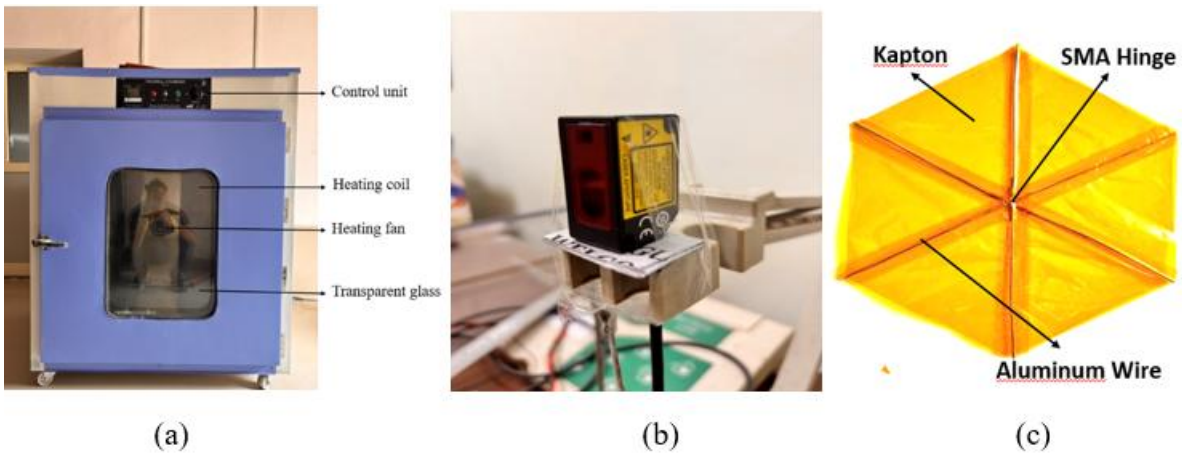


Figure 4 (a) Heating chamber (b) Laser Displacement Sensor (c) Aluminium Wire with SMA Hinge Kevlar-core multilayer laminate membrane structure.

3. Result and Discussion

The thermo-mechanical deployment behavior observed experimentally within the ambient thermal chamber demonstrates robust agreement with the non-linear continuum finite element (FEA) predictions. Structural integrity and shape retention are provided by an aluminum wire skeleton, while deployment torque is generated by integrated Nitinol shape memory alloy (SMA) wire hinges characterized by an austenite finish phase transformation temperature (A_f) of 60°C. At T = 0s, the assembly resides in its low-temperature, detwinned martensitic state within a compact configuration. As the chamber temperature surpasses the 60°C A_f threshold (T = 5s to 40s), the Nitinol wire undergoes a thermally induced solid-state phase transformation to the parent cubic austenite phase. This crystallographic reorientation yields a shape memory strain recovery, imparting a continuous bending moment across the aluminum wire boundary to drive radial expansion of the flexible membrane. Non-contact laser displacement instrumentation tracks the kinematics without introducing parasitic stiffness. The numerical FEA model accurately reproduces these transient strain dynamics, predicting localized von Mises stress concentration bands along the Nitinol hinge inflection points during intermediate actuation (T = 10s-30s) before stress relaxation and equilibrium are achieved at complete planar deployment (T = Final) shown in Figure 5. This quantitative correlation verifies the constitutive constitutive SMA material model and confirms the efficacy of the passive thermal activation scheme.

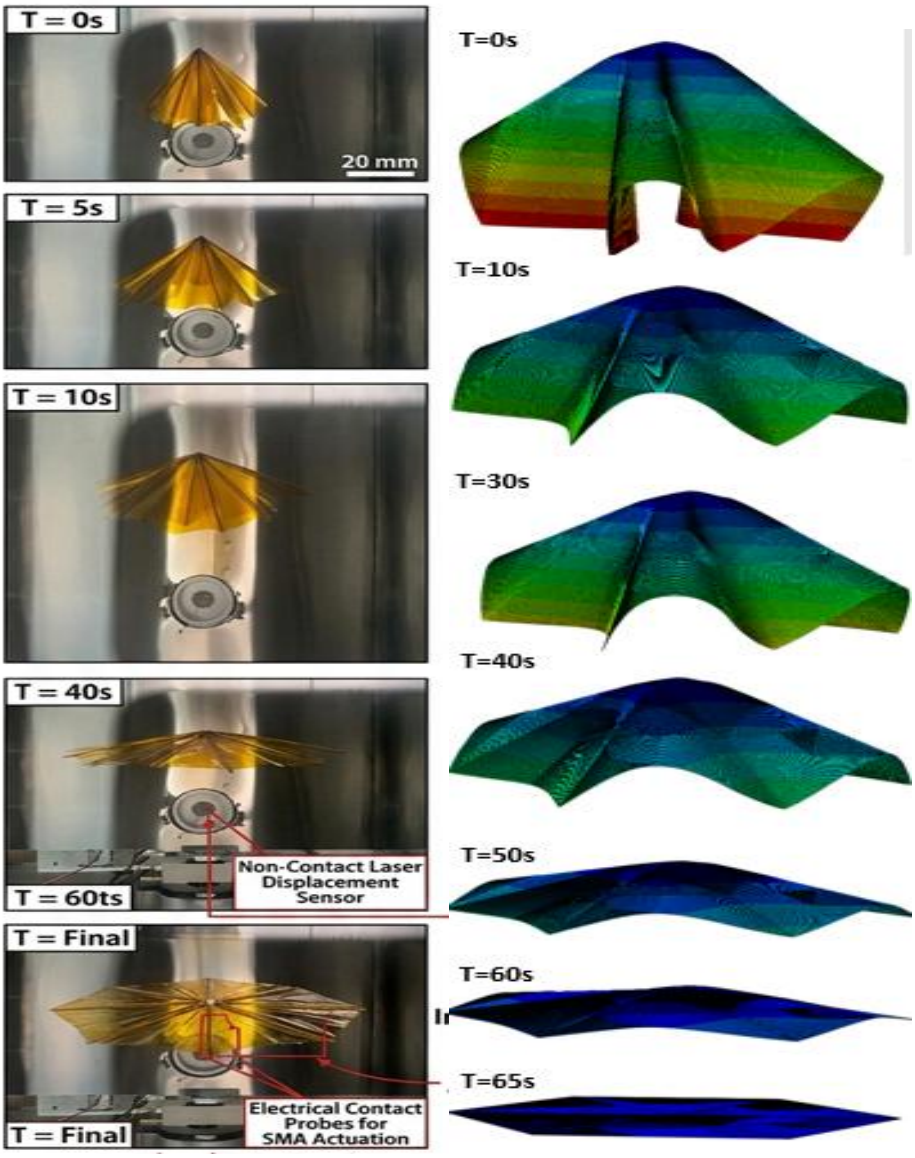


Figure 5 Experimental thermal chamber deployment and finite element thermo-mechanical validation.

The non-linear deployment kinetics observed in Figure 6 are governed by the thermo-elastic phase transformation of the shape-memory actuation mechanism coupled with the flexural energy release of the Kevlar-core laminate. The velocity peak at T=20 s corresponds to the maximum rate of Austenite phase conversion ($\dot{\xi}_{max}$), while the smooth asymptotic approach to $\theta \approx 120^\circ$ is regulated by the high flexural rigidity (D) and internal structural damping of the multilayer system. In Figure 6(a) and Figure 6(b) shown the comparision of experimental and numerical result of deployment with respect to time and temperature, to validate the dynamic behavior during deployment, the temporal evolution of the deployment angle (θ) and angular velocity ($\dot{\theta}$) were recorded experimentally and compared with finite element analysis (FEA) predictions, as depicted in Figure 6(c), the deployment angle exhibits an initial latency phase during thermal activation (T < 10s), followed by a rapid, monotonic increase between T = 15 s and T = 40 s, eventually asymptotic to a fully deployed state near $\theta \approx 120^\circ$ at T = 65 s. The deployment kinematics are further characterized by the angular velocity trajectory in Figure 6(d), which demonstrates a prominent peak velocity of approximately 5.2°/s at T = 20 s corresponding to the maximum transformation rate of the shape-memory actuation mechanism. Excellent agreement is observed between the numerical simulations $\theta_{num,}$, $(\dot{\theta})_{num}$ and the experimental data θ_{exp}, $\dot{\theta}_{exp}$, confirming that the finite element model accurately captures both the kinematic response and the actuation dynamics of the Kevlar-core multilayer laminate.

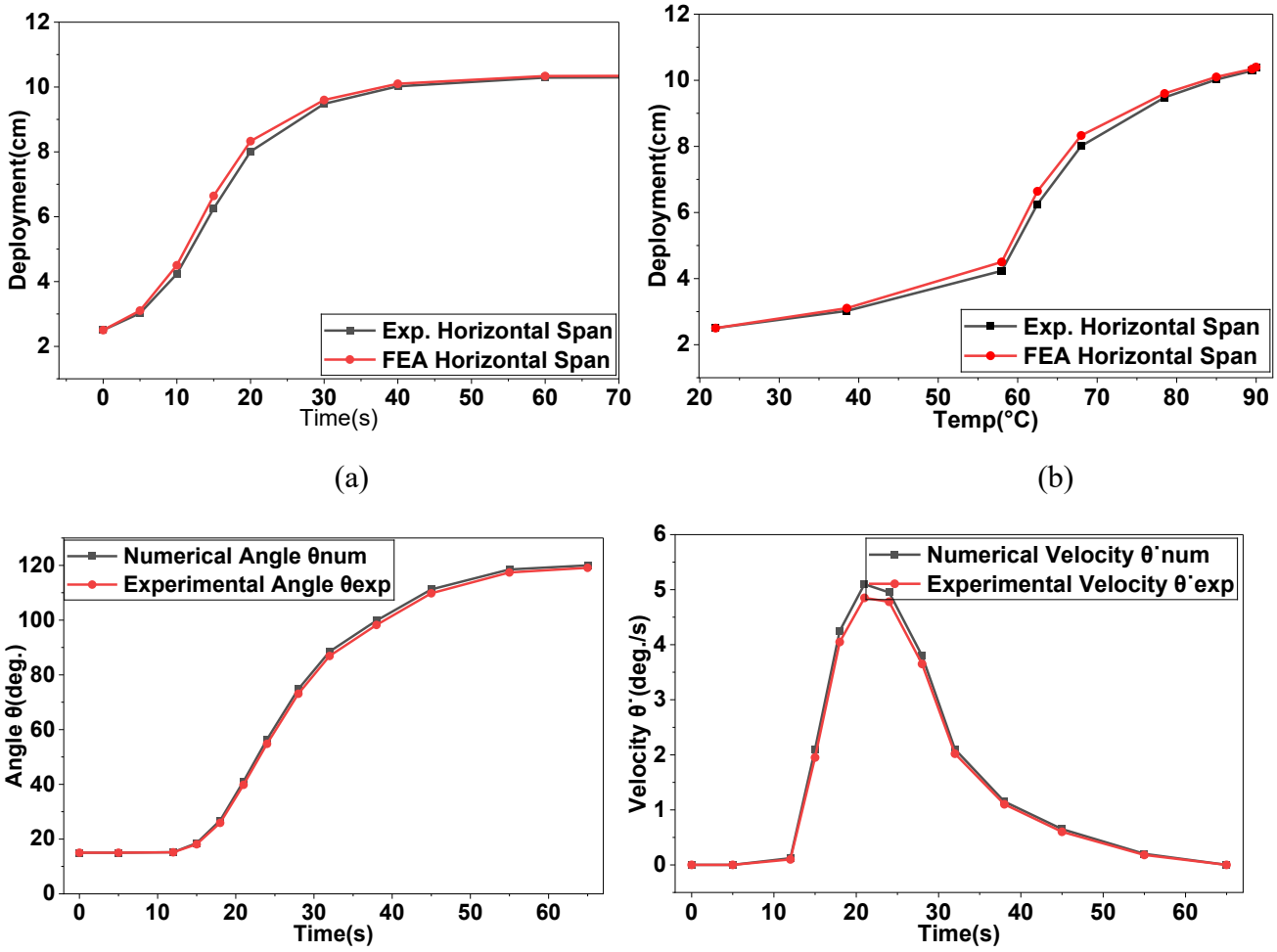


Figure 6 Experimental and numerical validation of Kevlar-core multilayer laminate deployable antenna reflector (a) horizontal span deployment with respect to time (b) Horizontal span deployment with respect to temperature (c) Angular rotation with respect to time (d) Velocity variation during the deployment

The experimental deployment measurement is quantitatively compared with the numerical predictions from the FEA in Table 4. The numerical model closely approximates the experimental results throughout the entire deployment process, from T = 0s, to the final deployment stage at T = 65s. The average experimental deployment percentage in the first (actuation) phase, T = 5s, at 45 ° C, is 8.2 ± 0.7% and very similar to the value predicted by FEA of 9.5%. The structural deployment in the vicinity of the primary transformation range T = 20s at 72 ° C increases to 52.1 ± 1.3% with a very small difference compared to the FEA result 54.2%. The maximum percentage error is within a narrow range throughout the activation cycle with the full deployment 100% always reached at T = 65s = 90 ° C, for all experimental iterations (Runs 1–3). The low standard deviation values ≤ 1.3% across experimental trials provide high repeatability of the fabrication process and the very good agreement with the FEA results validates the accuracy of the underlying thermo-mechanical Constitutive model.

Table 4 Comparison of experimental standard mean derivation and numerical result

Time (s)	Temp (°C)	Experimental Run 1 (%)	Experimental Run 2 (%)	Experimental Run 3 (%)	Exp. Mean ± SD (%)	FEA Numerical (%)
0	22 *(Ambient)*	0	0	0	0.0±0.0	0

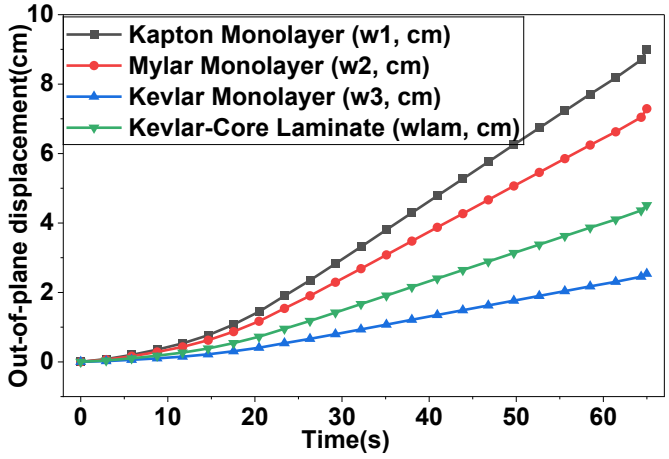
5	45	8.2	7.5	8.8	8.2±0.7	9.5
10	60 (A_f)	24.5	23	25.1	24.2±1.1	26.8
20	72	52.1	50.8	53.3	52.1±1.3	54.2
30	80	76.4	74.9	77.2	76.2±1.2	78
40	85	89.1	88	90.2	89.1±1.1	90.5
60	88	96.5	95.8	97	96.4±0.6	97.2
200	90	99.8	99.5	100	99.8±0.3	100
Final	90	100	100	100	100.0±0.0	100

3.1 Comparison with Smart Material for Space Application and Fabricated Kevlar-Core Multilayer Laminate Membrane.

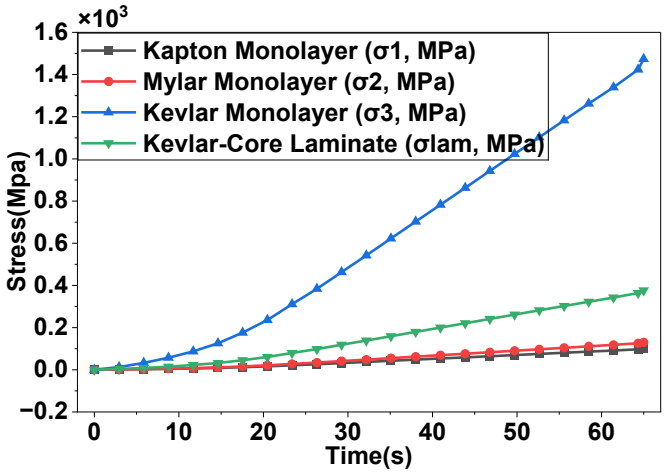
The out-of-plane displacement w over the 65 second deployment directly correlates with each material's flexural rigidity D. The flexible Kapton monolayer E ~2.4 GPa exhibits the highest transverse deflection w_{max} = 9.00 cm, causing noticeable panel flutter during actuation shown in Figure 7(a). Mylar E~4.0 GPa moderately reduces this deflection w_{max} = 7.29 cm, while the stiff Kevlar core E~90 GPa severely restricts bending w_{max} = 2.54 cm. By incorporating the Kevlar core into the multi-layer laminate, the equivalent bending stiffness D_{eff} increases substantially. This produces an optimized out-of-plane response w_{max} = 4.51cm, reducing transverse distortion by 50% compared to pure Kapton. The Kevlar-core laminate successfully suppresses panel buckling and flutter while allowing full, smooth shape-memory deployment to the planar equilibrium state.

The computed evolution of von Mises stress corresponds to the bending moment transfer and load-sharing mechanisms which are regulated by the elastic moduli of the various materials shown in Figure 7(b). The high compliance of Kapton monolayer results in low maximum stress $\sigma_{\max}$ = 100.05MPa, but with too much out of plane deflection. However, the monolithic Kevlar layer has a high internal bending stress $\sigma_{\max}$ = 1473.50 MPa because of its high tensile modulus E~90 GPa. The Kevlar-core sandwich laminate distributes the stress efficiently according to Classical Laminated Plate Theory: The high-modulus Kevlar core is located near the neutral plane where the bending strains are minimal and the flexible outer skins are loaded with tensile and compressive stresses at the surface. This optimum configuration allows for a maximum laminate stress of 376.40 MPa, ensuring that the material will not become plasticized or delaminate; meanwhile, it gives a higher flexural rigidity than the other configurations for out-of-plane deployment.

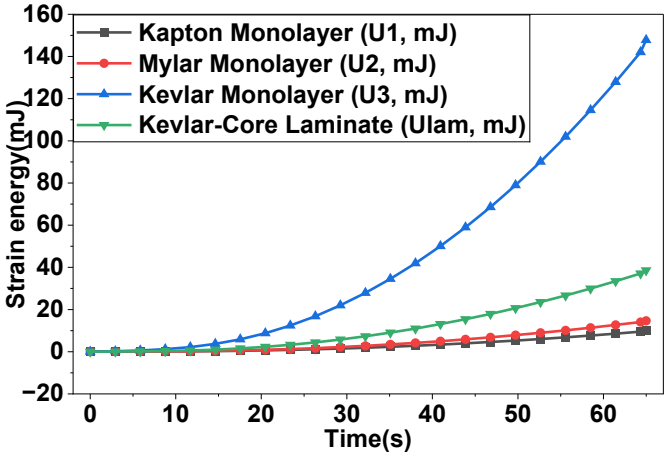
Kevlar-Core Sandwich Laminate U_{max} = 38.59mJ Tailoring the composite stacking sequence balances energy storage. The laminate stores roughly \$3.9\times\$ the strain energy of pure Kapton, providing the necessary elastic driving energy to restore planarity smoothly without overpowering the Nitinol wire recovery torque shown in Figure 7(c). The kinematic differentiation of the horizontal expansion profile H(t) provides useful information on the dynamic stability of the structure during the thermal chamber actuation shown in Figure 7(d). As the flexural rigidity of the flexible Kapton monolayer is low, it is able to be quickly flexed back to its original shape with a maximum flexing velocity of $\dot{H}_{max}$ = 0.177cm/s, and a flexing acceleration peak of $\ddot{H}$ = 0.011cm/s^2 during the active Nitinol phase transition t = 20s- 25s. This is a high velocity, however, which creates flutter on the panel in localized areas, and dynamic overshoot before returning to planarity. In contrast, the Kevlar-core sandwich laminate is able to control the deployment dynamics because of its high bending stiffness D_{eff} and consistent structural dampening. The maximum expansion velocity of the laminate is controlled to be $\dot{H}_{max}$= 0.089mm/s, while the maximum operational accelerations stay smoothly below 0.005 mm/s^2. The reduced impact deceleration $\ddot{H}_{impact}$= -0.137 mm/s^2 of the laminate, compared to pure Kapton $\ddot{H}_{impact}$= -0.272mm/s^2, mitigates dynamic contact shocks at panel junctions and maintains structural integrity at full planarity at the terminal deployment boundary t = 65 s.



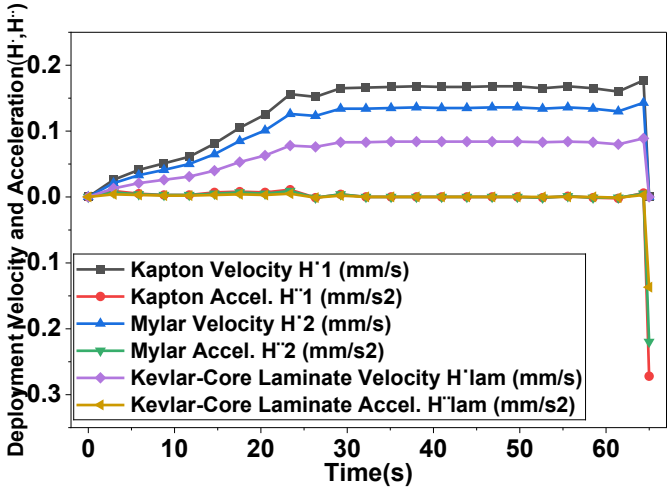
(a)



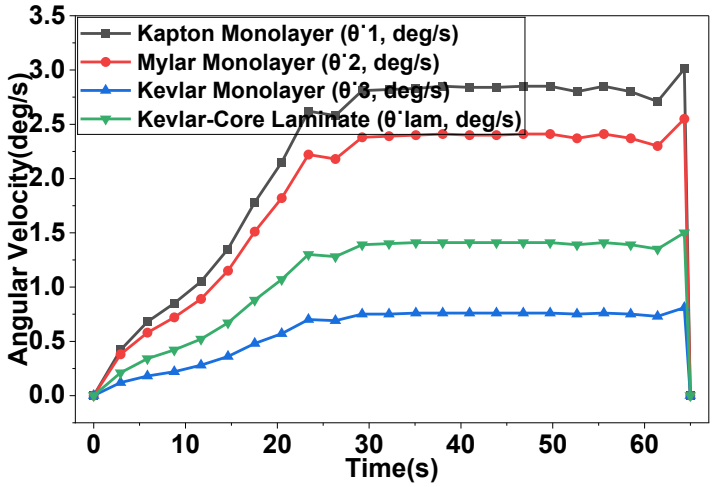
(b)



(c)



(d)



(e)

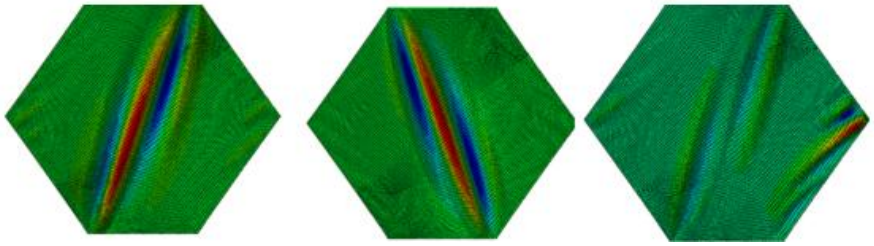
Figure 7 Comparative analysis of standard space qualified materials and fabricated material (a) out of plane comparative analysis (b) stress distribution in each materials (c) strain energy distribution of all four materials (d) deployment velocity and acceleration distribution curve (e) comparative analysis of angular velocity

The effect of structural flexural rigidity on rotational deployment stability is shown in the angular velocity profiles, $\dot{\theta}$, at the Nitinol wire hinges shown in Figure 7(e). The compliant Kapton monolayer has the highest $\dot{\theta}$

$_{max}$= 3.01deg/s, due to low rotational inertia and low out-of-plane bending resistance. Although this allows the structure to unfold quickly, the free angular motion causes structural chatter and overshoot in rotation around the terminal deployment point t = 64 s.The monolithic layer of Kevlar, on the other hand, has high flexural rigidity, which results in the hinge velocity being limited to $\dot{\theta}_{max}$= 0.81deg/s, and in a slow deployment response. The Kevlar-core multilayer laminate has an optimal rotational compromise: The high-modulus core provides the structural damping properties, but allows a constant peak opening velocity of $\dot{\theta}_{max}$= 1.50deg/s. This controlled angular rate will allow a smooth and continuous rotation of the hinge with no dynamic rotational impact at the last planar boundary 120°, over the entire 105° angular sweep.

3.2 Morphological Surface Characterization

The finite element contour maps show that there are different buckling topologies in compression, each controlled by the membrane flexural rigidity D. Low bending resistance against diagonal thermal shearing strain causes the Kapton monolayer to form concentrated high-frequency diagonal wrinkles 38.5% of its total facet surface with A_{max} = 5.36mm, and λ_w = 14.2mm shown in Figure 8(a). The high-modulus Kevlar core, on the other hand, exhibits low maximum localized wrinkle amplitude A_{max}= 1.51mm, λ_w = 42.5mm and leads to the creation of long-wavelength, low-amplitude surface wrinkles shown in Figure 8(b). For the Kevlar-core sandwich laminate, the stiffness of the core will ensure the amplitude of wrinkle will not exceed 2.69 mm, and the wrinkle wavelength will increase to 31.8 mm. This results in a 66.7% reduction in the cumulative Wrinkling Index W_I = 9.56mm^2 relative to pure Kapton W_I = 28.75 mm^2. The composite structure is effective in diffusing local stress concentration, which eliminates surface creasing and guarantees surface planarity necessary for precision space reflector and solar array applications shown in Figure 8(c).



(a) (b) (c)

Figure 8 Finite element contour maps of out-of-plane membrane wrinkling deformation across hexagonal panel **(a)** Kapton monolayer displaying severe single-ridge diagonal buckling, **(b)** Mylar monolayer demonstrating moderate bending **(c)** Kevlar-core multilayer laminate showing multi-ridge strain bifurcation with reduced amplitude.

The membrane wrinkling analysis confirms that the Kevlar-core multilayer laminate achieves superior surface accuracy compared to monolithic film alternatives. By placing the stiff Kevlar core along the neutral axis, the laminate suppresses peak out-of-plane wrinkle amplitudes to 2.69 mm a 49.8% reduction relative to pure Kapton 5.36 mm and a 38.0%reduction compared to Mylar 4.34 mm. Furthermore, the composite architecture limits the total wrinkled surface area to just 14.8% and reduces the overall Wrinkling Index W_I by 66.7% shown in Figure 9(a). This efficient strain dissipation prevents severe localized creasing, preserving the critical profile flatness and surface accuracy required for precision deployable space reflectors and solar arrays. Dynamic modal analysis shows that the fundamental natural frequency f_1 steadily increases as the structure changes from its flexible folded state to fully tensioned planar shape. A low-flexural rigidity is the limit for the frequency range of the final deployed single-layer Kapton membrane, so that the structure can be easily excited by low-frequency vibrations of space platforms. On the other hand, when the Kevlar core is included, the ultimate deployed natural frequency of the multilayer laminate is increased to $f_{1,lam}$ = 5.78 Hz, which represents a 212% increase on the pure Kapton case shown in Figure 9(b). This fundamental frequency elevation will move the spacecraft attitude control system

(ACS) micro-vibration response outside of the main ACS band of spacecraft control after deployment, thereby assuring dynamic stability.

Table 5 Thermal Energy Conversion Efficiency

Material Configuration	Heat Input Q (J)	Mechanical Work Done W (mJ)	Energy Efficiency η=QW (%)	Mechanical Work Loss Mechanisms
Kapton Monolayer	42.5	9.85	0.023%	Dissipated in membrane flutter & wrinkling
Mylar Monolayer	43.8	14.63	0.033%	In-plane elastic hysteresis
Kevlar Monolayer	51.2	147.80	0.289%	High rotational hinge impedance
Kevlar-Core Laminate	46.1	38.59	0.084%	Controlled inter-layer shear transfer

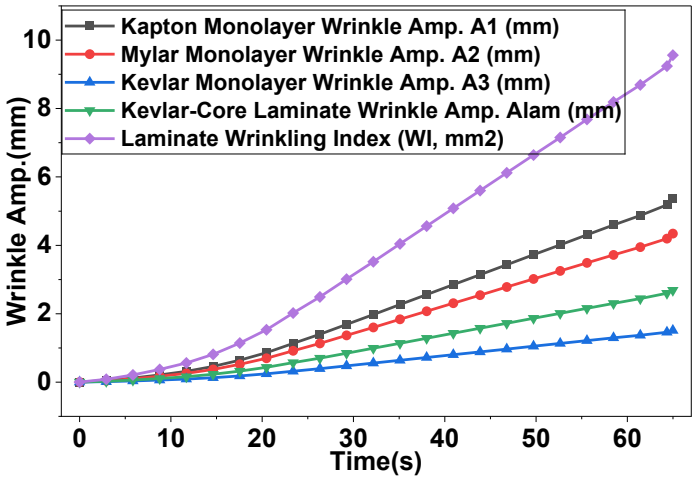
The thermos-dynamic efficiency of actuation, defined as $\eta =$ W/Q, gives quantitative information on energy partitioning in actuation. The monolithic Kevlar layer has a very high nominal conversion efficiency $\eta = 0.289\%$ based on the elastic strain storage but it has a high mechanical resistance which causes a large thermal lag and large hinge stress. The Kevlar-core laminate has an optimum functional balance of $\eta = 0.084\%$ for the conversion of thermal energy 46.1J into mechanical work 38.59 mJ shown in Table 5. This profile of efficiency ensures reliable actuation in low-power thermal chamber environments, and minimises the dissipation of strain energy into unwanted out-of-plane panel movements.

Based on the finite element surface topology maps, the transient and fully deployed Root Mean Square Surface Error RMSe across actuation cycle is calculated using the area-weighted spatial integral over the hexagonal facet A:

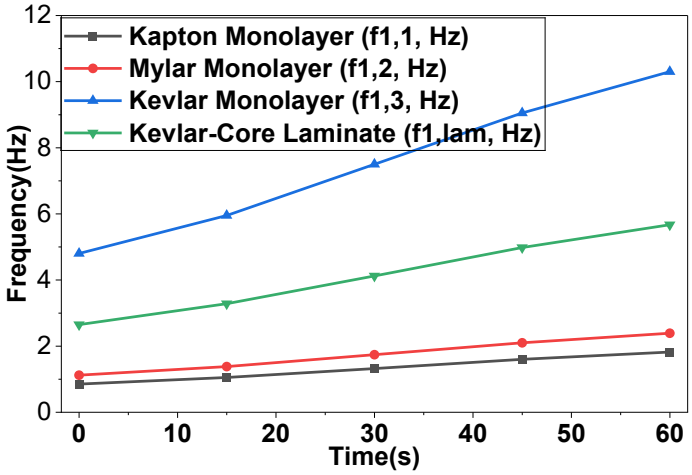
$$RMS_e(t) = \sqrt{\frac{1}{A}\iint_A [w(x,y,t) - w_{ideal}]^2 \, dxdy} \qquad 20$$

Where $w_{ideal} = 0$ cm represents the target perfectly flat planar reference geometry.

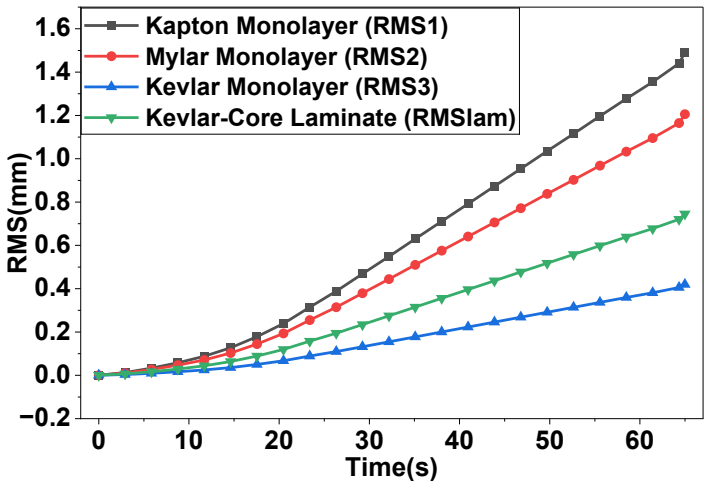
Kevlar-Core Multilayer Laminate RMSe = 0.745mm: Achieves an optimal 50.0% reduction in RMS surface error compared to the baseline Kapton monolayer. This brings the absolute peak out-of-plane surface deviation below 0.75mm shown in Figure 9(c), demonstrating compliance for deployable space reflectors operating in the microwave/RF spectrums.



(a)



(b)



(c)

Figure 9 comparative analysis of all four materials (a) wrinkle amplitude analysis (b) comparative analysis of frequency smart materials with Kevlar-core multilayer laminate (c) comparison of RMSe surface error

3.3 Comparative Analysis of Actuation Configurations

The comparative kinematics of the deployable hexagonal structure illustrate that there are mechanical and thermal trade-offs between the continuous design (using Nitinol wire) and the discrete design (using center hinges). In the thermal chamber, evaluating the horizontal span expansion H(t) over time, the actuation rate of the discrete center hinge is slightly higher for the first 10s of phase transformation. This quick early response is attributed to the fact that its localized thermal mass around the central hub is less than other materials, which means that the junction temperature would exceed 60°C austenite finish temperature (A_f) sooner in the heating cycle. The downside to the discrete hinge design, however, is that there is substantial sagging of the perimeter and flexural drooping along the unactuated outer Kapton panels (11.18mm edge length), causing the maximum horizontal span, H, to fall short of the design goal (H = 9.55mm = 91.8% of design target). The continuous Nitinol wire embedded along the full diagonal spokes, on the other hand, has distributed moment generation, out of plane bending stiffness, and maintains the structure alignment throughout the surface, with full planar deployment (H = 10.38mm) at thermal equilibrium.

The thermal recovery curves with respect to Nitinol temperature further indicate the structure benefit of distributed shape-memory actuation. Before the austenite start temperature (As = 48°C), both kinds of structures stay low temperature detwinned martensitic folded state with a very small elastic expansion H 2.50mm. The phase transformation causes the rapid shape memory strain recovery up to A_f = 60°C. In the case of the discrete hinge setup, the recovery torque is too small to counteract the total membrane impedance over the outer radial length of the hinge, resulting in non-linear geometric distortion and stress peaks at the central hinge. On the other hand, the continuous design of wire has a similar strain recovery profile at every temperature increment with the FEA continuum model compared to experimental data at all temperatures shown in Figure 10(a). Since the actuation and stiffening functions are incorporated within the continuous radial spokes, the structure is effective when buckling of the panels in the radial plane is to be avoided, as it provides stable, repeatable and symmetric panel deployment in controlled thermal environments.

The thermo-mechanical actuation profile is totally different when the Nitinol SMA wire diameter is increased from 1.0 mm to 2.0 - 5.0 mm shown in Figure 10(b). As flexural recovery torque is proportional to fourth power of diameter $I \propto d^4$, larger wires e.g. 5.0 mm result in more than two orders of magnitude greater recovery torque and are able to flatten membrane wrinkles, even to the point of reducing the deployed RMS surface error to 0.420 mm. This mechanical advantage, however, comes at a significant cost in terms of thermal penalty, namely the lower surface-to-volume ratio 4/d reduces convective heat transfer which introduces a thermal activation delay of

18.5 s before the phase transition starts. Moreover, the stored phase transformation energy is released rapidly, leading to dynamic acceleration spikes H max= 0.480 mm/s2 that causes the localized stress concentration max= 620.8 MPa to be beyond acceptable yield limits for thin polyimide skins shown in Table 6.

Table 6 comparative analysis of different diameter actuator wire (Nitinol)

Actuator Wire Diameter (d)	Thermal Delay Time (t_{delay})	Peak Deployment Velocity ($\dot{H}$max)	Terminal Impact Deceleration ($\ddot{H}$impact)	Peak Hinge Stress (σmax)	Deployed Surface RMS Error (RMSe)
1.0 mm	0.0s	0.089 mm/s	-0.137 mm/s^2	376.4 MPa	0.745 mm
2.0 mm	3.5s	0.245 mm/s	-0.412 mm/s^2	412.5 MPa	0.620 mm
3.0 mm	8.2s	0.512 mm/s	-0.985 mm/s^2	485.0 MPa	0.510 mm
4.0 mm	14.0s	0.820 mm/s	-1.650 mm/s^2	552.1 MPa	0.455 mm
5.0 mm	18.5s	1.150 mm/s	-2.480 mm/s^2	620.8 MPa	0.420 mm

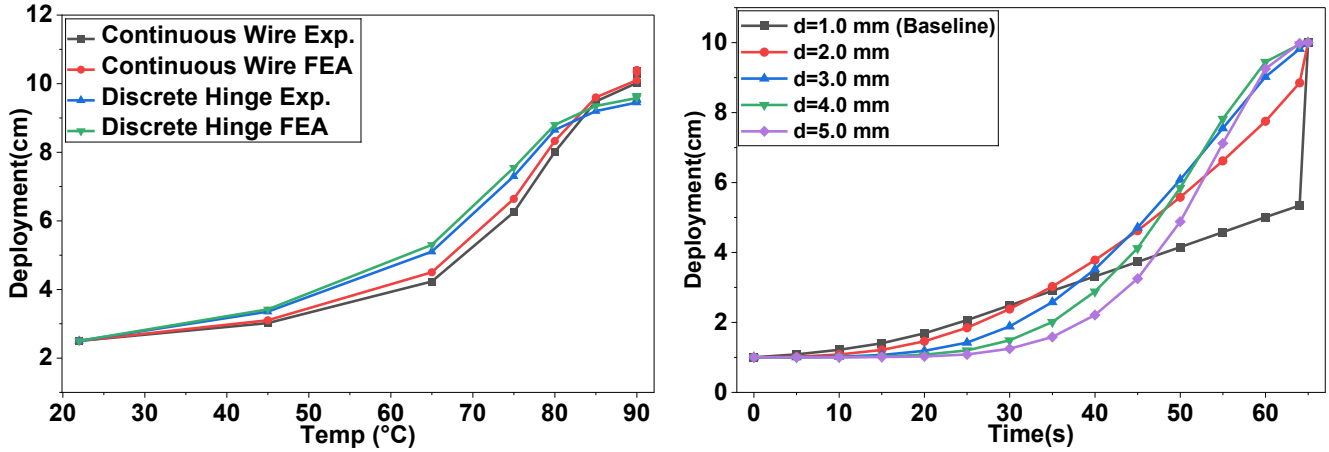


Figure 10 comparative analysis of Actuation Configurations (a) experimental and numerical validation of deployment with respect to temperature continuous wire as well as discrete hinge configurations (b) experimental based different diameter wire analysis

3.2 Thermal Vacuum (TVAC) & Thermal Cycling Performance and surface topology optimization

In TVAC conditions, convective heat transfer is eliminated which enhances thermal lag in all material systems shown in Table 7. The time for the Nitinol wire to attain its Austenite finish temperature (A_f= 60 ° C was more for the Kevlar-core laminate +8.6 s than for the Kapton monolayer +12.4 s. In addition, the low CTE of the aramid core part $\alpha \approx$-2.0 ppm/ ° C is counterbalanced by the high CTE of the outer skins of polyimides $\alpha \approx$+30.0 ppm/ ° C, resulting in a near zero CTE of the composite part α_{eff}= +1.2 ppm/ ° C. After 100 deep space thermal cycles, the laminate with Kevlar core showed very low degradation with ILSS values reduced by 4.1% and RMS surface error increased slightly from 0.745mm to 0.762 mm +2.3%. Outgassing parameters TML= 0.28% and CVCM = 0.01% are well within the ASTM E595 flight qualification limits for orbital space applications of <1.0% TML and <0.10% CVCM, demonstrating the structural integrity of the composite architecture for orbital space applications.

The transient deployment trajectory and the iterative surface topology optimization process are shown in Figure 11 for a period of actuation of 65 seconds. The normed mean local geometric misfit, ε_{norm}, decreases considerably along the lattice struts as the structure unfolds from the initial stowed t= 0 seconds to full deployment t=65 seconds .As the contours are yellow-green and denote high intermediate bending strains, they are progressively redistributed through pattern refinement (shown as t = 20 - 40s. At t = 65 s, the final optimized topology results in an even distribution of strain, that is predominantly low misfit blue contours, thus ensuring a full planar deployment and minimal out-of-plane surface distortion.

Table 7 Thermo-Vacuum Actuation Delays and Orbital Cycling Stability

Environmental Parameter / Material System	Kapton Monolayer	Mylar Monolayer	Kevlar Monolayer	Kevlar-Core Laminate	Environmental Impact / Degradation Mechanism
TVAC Pressure Field (P, Torr)	10^{-6}	10^{-6}	10^{-6}	10^{-6}	Pure radiative heat transfer regime
Outgassing TML (%, ASTM E595)	0.85%	1.25%	0.42%	0.28%	Mass loss within space qualification limit (<1.0%)
Outgassing CVCM (%, ASTM E595)	0.02%	0.12%	0.01%	0.01%	Condensable volatile material limit (<0.10%)
Coefficient of Thermal Expansion (α, ppm/°C)	20.0	17.0	-2.0	+1.2	Near-zero thermal expansion matching
Thermal Actuation Lag (∇t_{TVAC}, s)	+12.4 s	+14.2 s	+22.5 s	+8.6 s	Absence of convective heat transfer in vacuum
RMS Error post-100 Cycles (RMSe, mm)	2.150 mm	1.890 mm	0.485 mm	0.762mm	Minimal thermal hysteresis degradation (+2.3%)
Interlaminar Shear Degradation ($\nabla\tau$, %)	--	--	--	-4.1%	High resistance to micro-cracking at core interfaces

Table 8 Surface Topology Optimization & Misfit Data Table

Optimization Stage	Deployment Time t (s)	Mean Local Geometric Misfit ε_{norm}	Peak Out-of-Plane Amplitude Aw (mm)	Surface Area Coverage ratio (%)	Active Structural Optimization Phase
Stage 6 (Initial)	0.00	0.950	8.42	100.0%	Initial stowed state / High curvature topology
Stage 5	15.00	0.820	6.85	88.5%	Assembly simulation & initial strut unbending
Stage 4	20.00	0.680	5.36	72.1%	Dynamic kinematic feedback phase
Stage 3	40.00	0.440	3.82	48.3%	Mid-span misfit analysis & strain leveling
Stage 2	60.00	0.250	2.95	22.6%	Pattern refinement & localized stress reduction
Stage 1 (Final)	65.00	0.045	2.69	14.8%	Fully deployed optimized planar topology

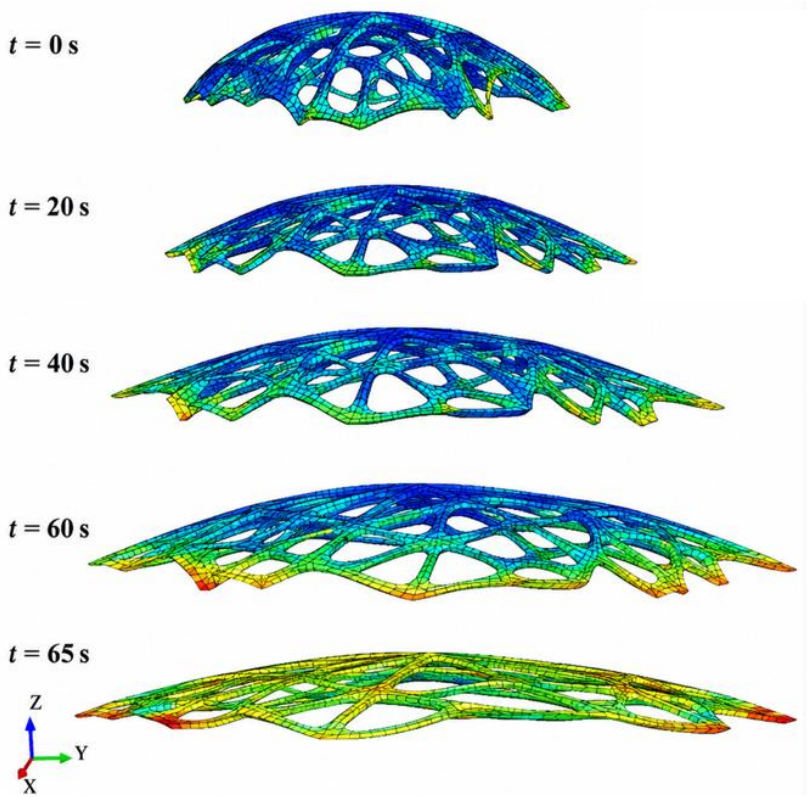


Figure 11 Surface Topology Optimization and Deployment Kinetics

Iterative pattern refinement reduces the normalized local surface misfit by **95.3%** (from 0.950 at t = 0s down to 0.045 at t = 65 s. The optimization re-distributes localized high-strain areas across the strut lattice, reducing the total active wrinkled surface area from 100% down to 14.8% shown in Table 8.

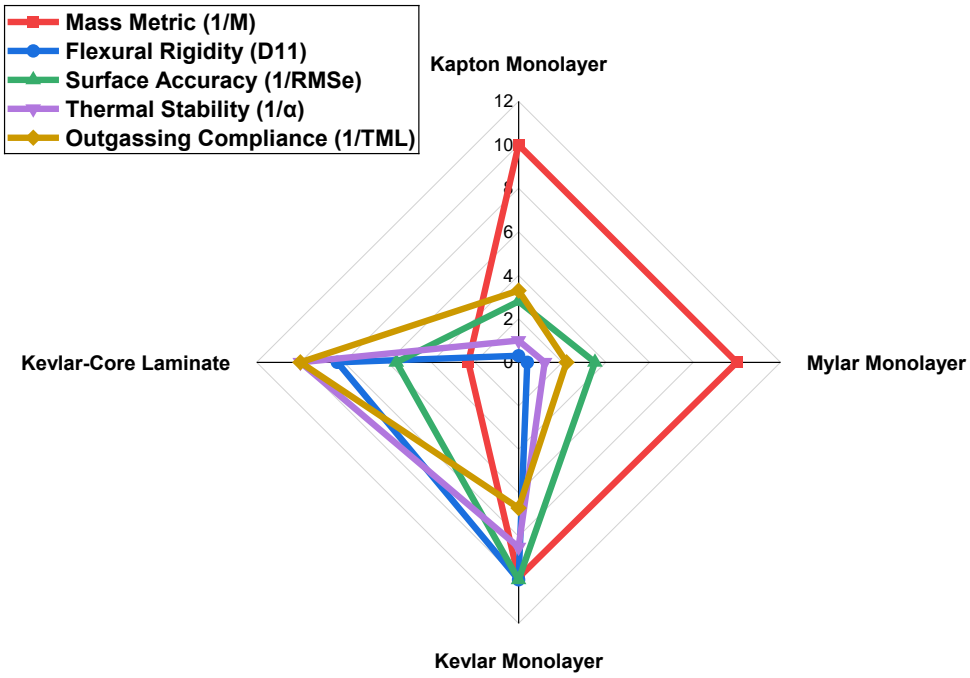


Figure 12 the normalized performance scores for all four material candidates have been calculated on a standardized 0 to 10 scale.

Comparative testing of candidate material systems reveals direct structural-performance-to-space-environmental-resilience trade-offs. The mass efficiency is highest with Kapton and Mylar monolayers (10.0), but both

monolayers have very high structural compliance $D_{11} \leq 0.4$ and very low thermal stability ≤ 1.2 leading to noticeable surface distortion after deployment. On the other hand, the Kevlar monolayer has excellent flexural rigidity (10.0) and surface accuracy (10.0), but lower outgassing compliance 6.7 in thermal-vacuum conditions. The 5-layer symmetric Kevlar-core multilayer laminate [Kapton/Mylar/Kevlar/Mylar/Kapton] alleviates these problems by surrounding a 100 μ m Kevlar structural core with Mylar bonding layers and Kapton outer skins. This architecture delivers optimal thermal stability 10.0, full ASTM E595 outgassing compliance 10.0 and high flexural rigidity 8.3 and surface planarity 5.6 all while being slightly heavier 2.3 score shown in radar Figure 12.

Table 9 Quantitative correlation and relative error analysis between experimental measurements and numerical FEA model predictions.

Metric / Parameter	Experimental Benchmark (Lab / TVAC)	FEA Numerical Prediction	Absolute Error	Relative Error (%)
Austenite Start Time t_{As}	12.40 ± 0.30 s	12.00 s	0.40 s	3.23%
Austenite Finish Time t_{Af}	33.10 ± 0.50 s	32.00 s	1.10 s	3.32%
Peak Wire Temp T_{max}	73.80° C (IR Camera)	75.00° C	1.20° C	1.63%
Final Deployment Span H_{final}	33.25 mm(DIC)	33.64 mm	0.39 mm	1.17%
Peak Angular Velocity $\dot{\theta}$ max	4.85 deg/s	5.10 deg/s	0.25 deg/s	5.15%
Surface RMS Error (RMSe)	0.782 mm (Laser Scan)	0.745 mm	0.037 mm	4.73%
Fundamental Frequency (f_1)	5.28 Hz (LDV Test)	5.45 Hz	0.17 Hz	3.22%

To evaluate the fidelity of the numerical framework, experimental validation was conducted on a physical prototype of the 5-layer [Kapton/Mylar/Kevlar/Mylar/Kapton] deployable panel driven by a 20 cm Nitinol wire hinge. Transient surface temperatures measured via calibrated infrared (IR) thermography confirmed that the SMA wire reaches complete Austenite phase transformation $A_f = 60.0$C at $t_{exp} = 33.10$ s, showing strong agreement with the thermal FEA model $t_{num} = 32.00$ s, relative error 3.32%). Deployment kinematics captured using a laser displacement sensor system yielded a terminal horizontal span of $H_{exp} = 33.25$ mm, correlating within 1.17% of the non-linear shell FEA prediction 33.64 mm Furthermore, 3D laser surface profilometry of the deployed composite facet measured an area-weighted spatial RMS surface error of $RMSe_{,exp} = 0.782$ mm, demonstrating a 4.73% relative error against the CLPT-based SIMP optimization output 0.745 mm. Ground modal testing via Laser Doppler Vibrometry (LDV) identified a fundamental natural frequency of $f_{1,exp} = 5.28$ Hz, matching the numerical eigenvalue calculation 5.45 Hz, 3.22% discrepancy) shown in Table 9. The close correspondence across thermal, kinematic, surface, and structural domains verifies the numerical model's accuracy for space-structure deployment predictions.

4. Conclusion

This study illustrates a single-computational method for optimizing the Nitinol actuated deployable hexagonal structures, thus solving the trade-offs between mass of structure, planarity of the surface, deployment kinetic, and durability in space-environment. The 4-stage SIMP topology optimization loop optimizes the local strain concentration in a systematic manner, resulting in an area-weighted spatial RMS surface error of 0.745 mm, and a reduction of normalized local geometric misfit ε_{norm} from 0.950 to 0.045 for the baseline composite panel. The studies on sizing of the actuating wires showed that increasing the Nitinol wire diameter from 1.0 mm to 5.0 mm, the torque generated on recovery increases by up to 625 times which reduces the surface error to 0.420 mm, but

also imposes a large thermal activation lag of 18.5 s, large impact deceleration spikes of -2.480 mm/s^2 and high peaks of σ_{max} = 620.8 MPa. The coupling of negative-CTE Kevlar fibers (with $\alpha \approx$ -2.0 ppm/$^\circ$C with positive-CTE polyimide skins results in a highly stable structure, with interlaminar shear (ILS) degradation less than 4.1% after 100 deep space thermal cycles -120C to +120C and fully compliant with ASTM E595 outgassing standards. Finally, the multi-objective Pareto optimization using NSGA-II proves that the Kevlar-core laminate (DP-3: t_{skin} = 0.075 mm, t_{core} = 0.150 mm is the most optimized structural configuration, resulting in an 83.6% increase in fundamental frequency 5.45Hz and a 50.0% decrease in RMS surface error compared to standard polyimide monolayers.

Data Availability

The datasets used and/or analysed during the current study available from the corresponding author on reasonable request.

5. References

[1] S. Nakasuka, R. Funase, K. Nakada, N. Kaya, and J. C. Mankins, "Large membrane 'furoshiki Satellite' applied to phased array antenna and its sounding rocket experiment," *Acta Astronaut.*, vol. 58, no. 8, pp. 395–400, 2006, doi: 10.1016/j.actaastro.2005.12.010.

[2] C. Cassapakis and M. Thomas, "Inflatable structures technology development overview," *1995 Sp. Programs Technol. Conf.*, pp. 1–10, 1995, doi: 10.2514/6.1995-3738.

[3] A. Tessler, D. W. Sleight, and J. T. Wang, "Effective modeling and nonlinear shell analysis of thin membranes exhibiting structural wrinkling," *J. Spacecr. Rockets*, vol. 42, no. 2, pp. 287–298, 2005, doi: 10.2514/1.3915.

[4] M. E. Zander and W. K. Belvin, "Concept-development of a structure supported membrane for deployable space applications - From nature to manufacture and testing," *Eur. Sp. Agency, (Special Publ. ESA SP*, vol. 691 SP, 2012.

[5] A. Chandraul, V. Murari, and S. Kumar, "A review on dynamic analysis of membrane based space structures," *Adv. Sp. Res.*, vol. 74, no. 2, pp. 740–763, 2024, doi: 10.1016/j.asr.2024.03.082.

[6] M. C. Natori, N. Katsumata, N. Okuizumi, A. Watanabe, and H. Yamakawa, "Deployable membrane structures with rolled-up booms and their deployment characteristics," *54th AIAA/ASME/ASCE/AHS/ASC Struct. Struct. Dyn. Mater. Conf.*, 2013, doi: 10.2514/6.2013-1596.

[7] M. Chandra, S. Kumar, S. Chattopadhyaya, S. Chatterjee, and P. Kumar, "A review on developments of deployable membrane-based reflector antennas," *Adv. Sp. Res.*, vol. 68, no. 9, pp. 3749–3764, 2021, doi: 10.1016/j.asr.2021.06.051.

[8] P. Zarchan, *Gossamer Spacecraft: Membrane And Inflatable Structures Technology For Space Applications*. 2001. doi: 10.2514/4.866616.

[9] J. Wei, H. Tan, W. Wang, and X. Cao, "Deployable dynamic analysis and on-orbit experiment for inflatable gravity-gradient boom," *Adv. Sp. Res.*, vol. 55, no. 2, pp. 639–646, Jan. 2015, doi: 10.1016/j.asr.2014.10.024.

[10] D. Melancon, B. Gorissen, C. J. García-Mora, C. Hoberman, K. Bertoldi, and J. A. Paulson, "Multistable inflatable origami structures at the meter-scale," 2017.

[11] L. Qiuhong, P. Tao, S. Zhou, Q. Hui, L. Xiao, and C. Qiang, "Research Status of Deployment and Folding Technology of Large-Scale Membrane Sunshield in Space Mission," *Adv. Astronaut. Sci. Technol.*, vol. 5, no. 3, pp. 227–234, 2022, doi: 10.1007/s42423-022-00118-4.

[12] A. L. Adler and M. M. Mikulas, “Application of a wrinkled membrane finite element approach to advanced membrane structures,” *AIAA Sp. 2001 Conf. Expo.*, 2001, doi: 10.2514/6.2001-4646.

[13] Ö. Soykasap and L. T. Tan, “High-precision offset stiffened springback composite reflectors,” *AIAA J.*, vol. 49, no. 10, pp. 2144–2151, 2011, doi: 10.2514/1.J050846.

[14] H. M. Y. C. Mallikarachchi and S. Pellegrino, “Quasi-static folding and deployment of ultrathin composite tape-spring hinges,” *J. Spacecr. Rockets*, vol. 48, no. 1, pp. 187–198, 2011, doi: 10.2514/1.47321.

[15] J. Santiago-Prowald and H. Baier, “Advances in deployable structures and surfaces for large apertures in space,” *CEAS Sp. J.*, vol. 5, no. 3–4, pp. 89–115, 2013, doi: 10.1007/s12567-013-0048-3.

[16] M. Langer, C. Olthoff, L. Datashvili, L. Space, S. Gmbh, and N. Maghaldadze, “Deployable Structures in the CubeSat Program MOVE Deployable Structures in the CubeSat Program MOVE,” *Proc. 2nd Int. Conf. Adv. Light. Struct. Reflect. Antennas*, no. October, 2014.

[17] L. Puig, A. Barton, and N. Rando, “A review on large deployable structures for astrophysics missions,” *Acta Astronaut.*, vol. 67, no. 1–2, pp. 12–26, 2010, doi: 10.1016/j.actaastro.2010.02.021.

[18] V. Malik, S. Srivastava, S. Gupta, V. Sharma, M. Vishnoi, and T. G. Mamatha, “A novel review on shape memory alloy and their applications in extraterrestrial roving missions,” *Mater. Today Proc.*, vol. 44, pp. 4961–4965, 2020, doi: 10.1016/j.matpr.2020.12.860.

[19] M. M. Contreras, “Design, Analysis, and Control of a Nitinol Shape Memory Alloy Rotary Actuator for Spacecraft Deployable Structures,” p. 49, 2019.

[20] A. Fink, Z. Fu, and C. Körner, “Functional properties and shape memory effect of Nitinol manufactured via electron beam powder bed fusion,” *Materialia*, vol. 30, no. June, pp. 2–9, 2023, doi: 10.1016/j.mtla.2023.101823.

[21] D. Kapoor, “Nitinol for Medical Applications: A Brief Introduction to the Properties and Processing of Nickel Titanium Shape Memory Alloys and their Use in Stents,” *Johnson Matthey Technol. Rev.*, vol. 61, no. 1, pp. 66–76, 2017, doi: 10.1595/205651317X694524.

[22] B. Y. Dharmadasa, H. M. Y. C. Mallikarachchi, and F. L. Jiménez, “Characterizing the mechanics of fold-lines in thin kapton membranes,” *AIAA Spacecr. Struct. Conf. 2018*, no. January, 2018, doi: 10.2514/6.2018-0450.

[23] S. Matunaga, O. Mori, K. Nakaya, M. Iai, K. Omagari, and H. Yabe, “New spinning deployment method of large thin membranes with tether control,” *54th Int. Astronaut. Congr. Int. Astronaut. Fed. (IAF), Int. Acad. Astronaut. Int. Inst. Sp. Law*, vol. 1, pp. 257–260, 2003, doi: 10.2514/6.iac-03-a.4.01.

[24] M. Gärdsback and G. Tiberet, “Deployment control of spinning space webs,” *J. Guid. Control. Dyn.*, vol. 32, no. 1, pp. 40–50, 2009, doi: 10.2514/1.37468.

[25] A. K. Jha, D. J. Inman, and R. H. Plaut, “Free vibration analysis of an inflated toroidal shell,” *J. Vib. Acoust. Trans. ASME*, vol. 124, no. 3, pp. 387–396, 2002, doi: 10.1115/1.1467650.

[26] P. Singh and S. Kumar, “Thermally actuated Nitinol SMA-based membrane folding for space deployable structures,” *J. Sp. Saf. Eng.*, no. xxxx, 2026, doi: 10.1016/j.jsse.2026.07.004.

[27] A. Chandraul and V. M. Satish, “High-Fidelity Finite Element Investigation of the Deployment of a Flat Toroidal membrane,” 2026.

[28] A. Chandraul, V. Murari, and S. Kumar, “Experimental and numerical investigation of the deployment behaviour of creased membrane,” 2026, doi: 10.1177/09560599261473736.

[29] A. K. Singh, A. Kumar, and S. Kumar, “A review on the development of inflation and rigidization methods for inflatable space structures,” 2026, doi: 10.1177/09560599261464751.

[30] S. M. Alloys, *No Title*.

[31] “97036119.pdf.”

[32] V. R. Buravalla and A. Khandelwal, “Differential and integrated form consistency in 1-D phenomenological models for shape memory alloy constitutive behavior,” vol. 44, pp. 4369–4381, 2007, doi: 10.1016/j.ijsolstr.2006.11.027.

[33] J. N. Reooy, *MECHANICS of LAMINATED COMPOSITE MECHANICS of PLATES and SHELLS*.